

ARTICLE

Open Access

High-performance sodium-ion hybrid capacitors based on an interlayer-expanded MoS₂/rGO composite: surpassing the performance of lithium-ion capacitors in a uniform system

Changzhen Zhan¹, Wei Liu¹, Mingxiang Hu^{1,2}, Qinghua Liang¹, Xiaoliang Yu^{1,3}, Yang Shen¹, Ruitao Lv^{1,2}, Feiyu Kang^{2,3} and Zheng-Hong Huang^{1,2}

Abstract

Hybrid supercapacitors (HSCs) are novel, promising devices having features of both batteries and supercapacitors. Herein, we report HSCs (Li-HSC and Na-HSC in a uniform system) based on an interlayer-expanded MoS₂/rGO composite that show ultrahigh energy density and power density as well as superior cycle stability. The 3D network-structured interlayer-expanded MoS₂/rGO nanocomposite (3D-IEMoS₂@G) was synthesized and employed as the anode. Because the 3D architecture of the graphene skeleton frame delivered sufficient charges and the highly interlayer-expanded MoS₂ achieved fast ion diffusion, the as-prepared composite exhibited excellent performance as the anode material for both LIBs and SIBs (1600 mAh g⁻¹ at 100 mA g⁻¹ for the LIB; 580 mAh g⁻¹ at 100 mA g⁻¹ and 320 mAh g⁻¹ at a high current density of 10 A g⁻¹). When paired with nitrogen-doped hierarchically porous 3D graphene (N-3DG), the obtained Na-HSC surpassed Li-HSC in a uniform system, showing an excellent performance of 140 Wh kg⁻¹ at 630 W kg⁻¹, 43 Wh kg⁻¹ at an ultrahigh power density of 103 kW kg⁻¹ (charge finished within 1.5 s) and no distinct capacity attenuation after over 10000 cycles. Thus, a quantitative kinetic analysis was performed to understand the synergistic effect of the two electrodes and the resulting effect of ions in the hybrid supercapacitors and to further pave a general path for fabricating high-performance HSCs.

Introduction

Energy storage has attracted unprecedented attention in recent years, and high-performance energy storage devices are under great demand¹. Currently, there are two types of dominating electrical energy storage devices: secondary batteries and supercapacitors. Secondary batteries store energy through a Faradic process, thereby

attaining high energy density but weak kinetics performance². Lithium-ion batteries (LIBs), for example, can exhibit an energy density >150 Wh kg⁻¹ but show unpromising power density (<1000 W kg⁻¹) and poor cycle stability (~1000 cycles)³. In contrast, supercapacitors (electronic double layer capacitors (EDLCs)) store energy through a non-Faradic process (electrostatic charge adsorption), which leads to ultrahigh power density (~10 kW kg⁻¹) and cycle stability (more than 10,000 cycles) but also low energy density (5–10 Wh kg⁻¹)⁴. However, neither of these can currently meet the great demand for devices with both high energy density and high power density for electric vehicles and electronic devices.

Correspondence: Zheng-Hong Huang (zhhuang@mail.tsinghua.edu.cn)

¹State Key Laboratory of New Ceramics and Fine Processing, School of Materials Science and Engineering, Tsinghua University, 100084 Beijing, China

²Key Laboratory of Advanced Materials (MOE), School of Materials Science and Engineering, Tsinghua University, 100084 Beijing, China

Full list of author information is available at the end of the article.

© The Author(s) 2018



Open Access This article is licensed under a Creative Commons Attribution 4.0 International License, which permits use, sharing, adaptation, distribution and reproduction in any medium or format, as long as you give appropriate credit to the original author(s) and the source, provide a link to the Creative Commons license, and indicate if changes were made. The images or other third party material in this article are included in the article's Creative Commons license, unless indicated otherwise in a credit line to the material. If material is not included in the article's Creative Commons license and your intended use is not permitted by statutory regulation or exceeds the permitted use, you will need to obtain permission directly from the copyright holder. To view a copy of this license, visit <http://creativecommons.org/licenses/by/4.0/>.

Hybrid supercapacitors (HSCs), which are novel devices with the good features of both batteries and supercapacitors, have recently attracted increasing scientific attention^{5,6}. HSCs are constituted by a battery-type electrode and a supercapacitor-type electrode. Take a lithium-ion HSC (Li-HSC) as an example, activated carbons (ACs) are commonly employed as the supercapacitor-type electrode, storing energy by electrostatic charge adsorption^{5,7}, and many LIB anode materials (such as graphite⁵ and $\text{Li}_4\text{Ti}_5\text{O}_{12}$ ⁷) have been examined as the battery-type electrode, proceeding an ion intercalation and deintercalation reaction during charge/discharge cycling. The energy density of HSCs is codetermined by the specific capacity and voltage window⁶. In HSCs, the electric potential of the positive electrode (supercapacitor-type) is restricted by decomposition of the electrolyte; therefore, a high energy density can be obtained by employing a battery-type anode material with both high capacity and low potential. For instance, Li-HSCs paired with AC and a low-potential anode (graphite⁵, Fe_3O_4 ⁸, SnO_2 ⁹, hard carbon¹⁰, etc.) have achieved a high voltage window of over 4 V and high energy density of over 100 Wh kg^{-1} . However, the power performance was restricted by the ion diffusion limitations of the battery-type electrode. Hence, anode materials with high capacity, low potential and, more importantly, effective architecture facilitating rapid ion and electron transport are key factors in fabricating high-performance HSCs with beneficial electrochemical properties.

Two-dimensional materials have been widely studied in the field of energy storage due to their fascinating and unique properties¹¹. For instance, graphene, due to its excellent electronic conductivity and high specific surface area (SSA), has been applied on its own as an EDLC electrode material and as a skeleton in composite electrode materials¹². Transition metal dichalcogenides (TMDs), such as MoS_2 ³, WS_2 ¹³, and SnS_2 ¹⁴, have been reported as host electrode materials for rechargeable batteries owing to their layered structure, which allows the intercalation of foreign atoms or alkali metals. Typically, when used as anode for LIBs or SIBs, MoS_2 exhibits a high capacity and low potential, demonstrating its potential as a HSC battery-type electrode. However, to the best of our knowledge, few studies have reported TMD-based Li-HSCs or sodium-ion HSCs (Na-HSCs), probably because of their unpromising ion and electron transport properties. Therefore, to construct a HSC with ideal performance, the modification of MoS_2 materials is essential. Expanding the interlayer spacing, which decreases the ion diffusion pathways and increases the active area, is an effective method to enhance the power performance of the host electrode¹⁵. On the other hand, combination with carbon materials is a promising method to construct effective paths for ion diffusion and electron

transport^{16,17}. For example, Chen's group reported layered MoS_2 /graphene composites synthesized through a facile process with the assistance of L-cysteine, which showed excellent electrochemical performance as anode materials for LIBs¹⁸. Piao's group reported a scalable strategy for synthesizing few-layer MoS_2 incorporated into hierarchical porous carbon nanosheet composites, which exhibited excellent electrochemical performance as anode materials for both LIBs and SIBs¹⁹. Meanwhile, introducing a heterostructure between layered 2D MoS_2 and graphene could introduce synergistic effects that are of great benefit to enhancing the overall performance of the composite material²⁰.

Recently, with the rapid increase in the scale of energy storage, sodium-based energy storage systems have gained increasing attention due to the abundance and low cost of sodium². Nevertheless, there are still many challenges to overcome before SIBs can be commercialized. For example, the radius of Na^+ is much larger than that of Li^+ ; therefore, it is difficult to find suitable host materials for reversible SIBs²¹. Namely, there is currently a distinct gap in the overall electrochemical performance of sodium-based and lithium-based energy storage devices²². In a HSC, the disadvantage of Na^+ versus Li^+ exists in only one electrode. Hence, the gap between Na-HSCs and Li-HSCs is narrower than that in battery systems, and Na-HSCs are a feasible approach to achieving an energy storage device with good performance at low cost²³.

In this work, we successfully synthesized a well-structured 3D interlayer-expanded MoS_2 /rGO nanocomposite (3D-IEMoS₂@G). Because the 3D architecture of the graphene skeleton frame delivered sufficient charges and the highly interlayer-expanded MoS_2 achieved fast ion diffusion, the as-prepared well-structured composite exhibited excellent performance as anode materials for both LIBs and SIBs (1600 mAh g^{-1} at 100 mA g^{-1} for LIBs; 580 mAh g^{-1} at 100 mA g^{-1} and 320 mAh g^{-1} at a high current density of 10 A g^{-1}). When paired with nitrogen-doped hierarchically porous 3D graphene (N-3DG), the fabricated HSCs (Li-HSC and Na-HSC) showed ultrahigh energy density, power density and superior cycle stability. In particular, the obtained Na-HSC showed 140 Wh kg^{-1} at 630 W kg^{-1} , 43 Wh kg^{-1} at an ultrahigh power density of 103 kW kg^{-1} (charge finished within 1.5 s) and no distinct capacity attenuation after over 10,000 cycles. Moreover, a quantitative kinetic analysis was performed to understand the synergistic effect of the two electrodes and the resulting effect of ions in the HSCs, as well as to determine a general path for fabricating high-performance HSCs.

Materials and methods

Synthesis of 3D-IEMoS₂@G

A well-structured 3D interlayer-expanded MoS_2 /graphene (3D-IEMoS₂@G) nanocomposite was prepared by a

one-step in situ solvothermal process. In brief, graphite oxide (Institute of Coal Chemistry, Chinese Academy of Sciences) was dispersed in dimethyl formamide (DMF) at 4 mg ml^{-1} with ultrasonic treatment for 2 h. Then, 200 mg ammonium tetrathiomolybdate (ATTM) was dissolved in 10 ml DMF and stirred for several minutes. The solution was mixed with 15 ml fresh GO DMF dispersion with further ultrasonic processing for 0.5 h and then transferred into a 60 ml Teflon-lined autoclave. The tightly sealed autoclave was heated to $190 \text{ }^\circ\text{C}$ at a rate of $5 \text{ }^\circ\text{C min}^{-1}$ in an oven and maintained for 18 h. After the autoclave cooled to room temperature naturally, the fragile sponge-like 3D-MoS₂@G was carefully transferred into a beaker containing deionized (DI) water. The DI water steeped in the sample was then exchanged several times in the following two days with DMF and then with DI water. Lastly, the sponge-like 3D-MoS₂@G swollen with water was vacuum freeze dried for 24 h. For comparison, pure solvothermal MoS₂ (S-MoS₂) and graphene (S-G) were prepared by the same process through a solvothermal reaction of ATTM or GO dispersion. Annealed 3D-IEMoS₂@G samples were prepared by annealing 3D-IEMoS₂@G in Ar atmosphere at $800 \text{ }^\circ\text{C}$ for 1 h.

Synthesis of nitrogen-doped 3D graphene

N-3DG was prepared as follows: 60 ml 2 mg ml^{-1} GO aqueous dispersion was placed in a 100 ml Teflon-lined autoclave. The autoclave was heated at $120 \text{ }^\circ\text{C}$ in an oven and maintained for 12 h. The obtained sponge-like 3D graphene was vacuum freeze dried and then heated to $750 \text{ }^\circ\text{C}$ at a rate of $5 \text{ }^\circ\text{C min}^{-1}$ in a tube furnace under Ar atmosphere and held for 0.5 h under ammonia atmosphere for further activation and nitrogen doping. For comparison, 3D graphene (3DG) without nitrogen doping was prepared by the same process, except it was heated at $750 \text{ }^\circ\text{C}$ for 0.5 h under Ar instead of ammonia.

Characterization methods

Scanning electron microscopy (SEM, LEO1530) and transmission electron microscopy (TEM, Tecnai G20, 200 kV) were used to characterize the samples. N₂ sorption isotherms were measured using a volume adsorption apparatus at 77 K. The total pore volume was estimated from the single-point adsorption ($P/P_0 = 0.995$), the SSA was calculated by the Brunauer-Emmett-Teller (BET) method, the micropore surface area and micropore volume were determined by the t-plot method, and the pore size distribution (PSD) was derived from density functional theory (DFT). X-ray photoelectron spectroscopy (XPS, PHI Quantera Imaging) was used to investigate the surface chemistry. The material phases were examined by X-ray diffraction (XRD, Bruker D8 ADVANCED) operating at an acceleration voltage of 40 kV. The structure was determined

by Raman spectroscopy (Renishaw, InVia-Reflex) using a 532 nm laser.

Fabrication of the cells

The electrode materials were mixed with 10% PVDF, 10% carbon black (Super P) and excess NMP solvent to obtain a homogeneous slurry. Then, the slurry was coated on aluminum foil to prepare the cathode materials and on copper foil to prepare the anode materials. The foils were dried at $80 \text{ }^\circ\text{C}$ for 4 h and then at $120 \text{ }^\circ\text{C}$ in vacuum for 12 h. The electrodes were punched into disks with a diameter of 12 mm for electrochemical tests. The mass loading of the cathode electrodes was controlled at 4 mg for the symmetric supercapacitors and HSC. The mass loading of the anode electrodes was fixed at $\sim 2 \text{ mg}$ in half cells and adjusted individually in HSCs to fulfill the given mass ratio of two electrodes. LIB and SIB half cells were assembled using a lithium/sodium metal electrode and an active material. Symmetric supercapacitors were assembled by two porous electrodes with equal masses of active material. HSCs were assembled by coupling N-3DG and 3D-IEMoS₂@G. All devices were fabricated into 2032 coin cells, and the electrolyte used in the half cells and HSCs was 1 M LiPF₆ and NaClO₄ in EC/DMC (1:1 by volume), respectively.

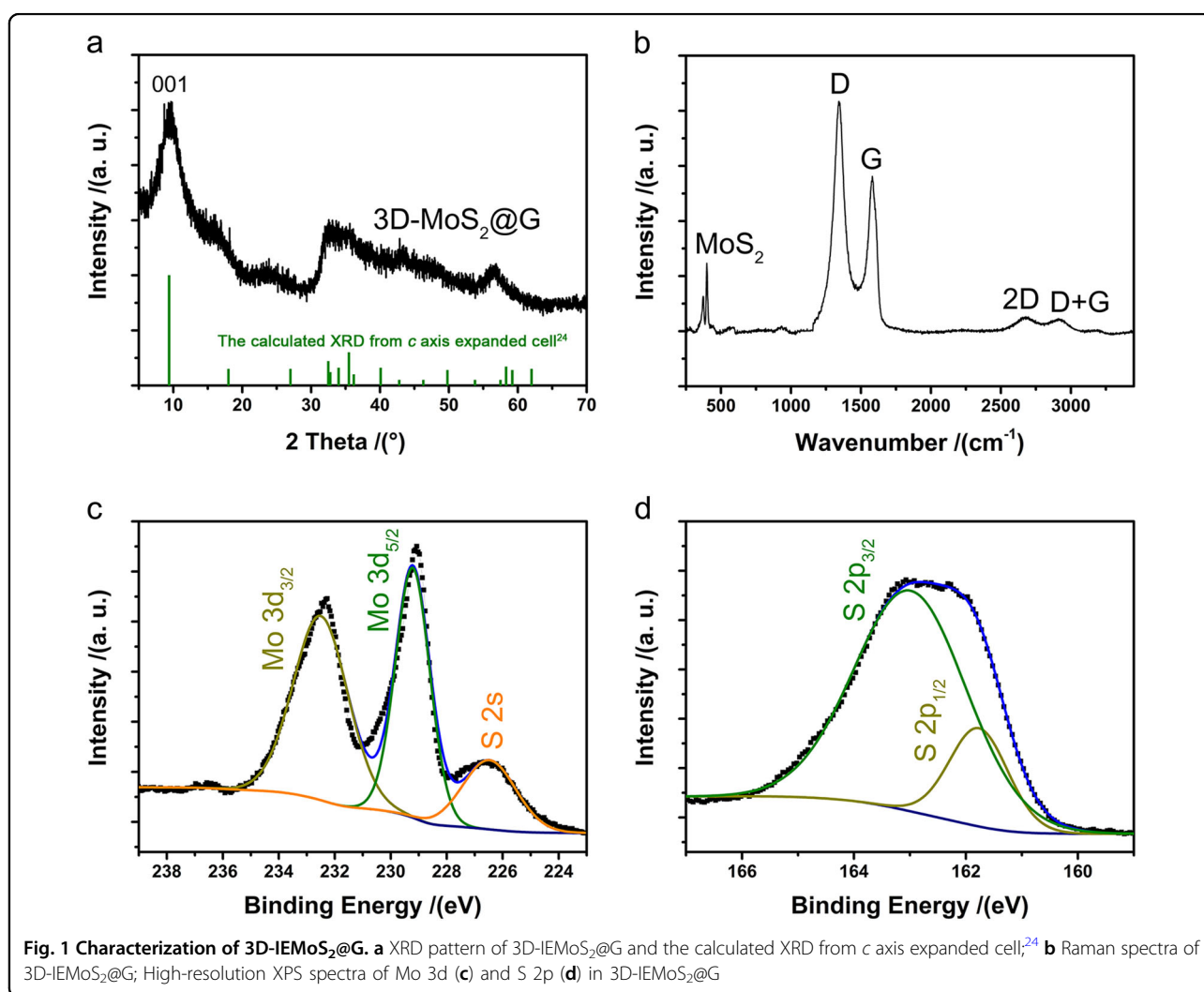
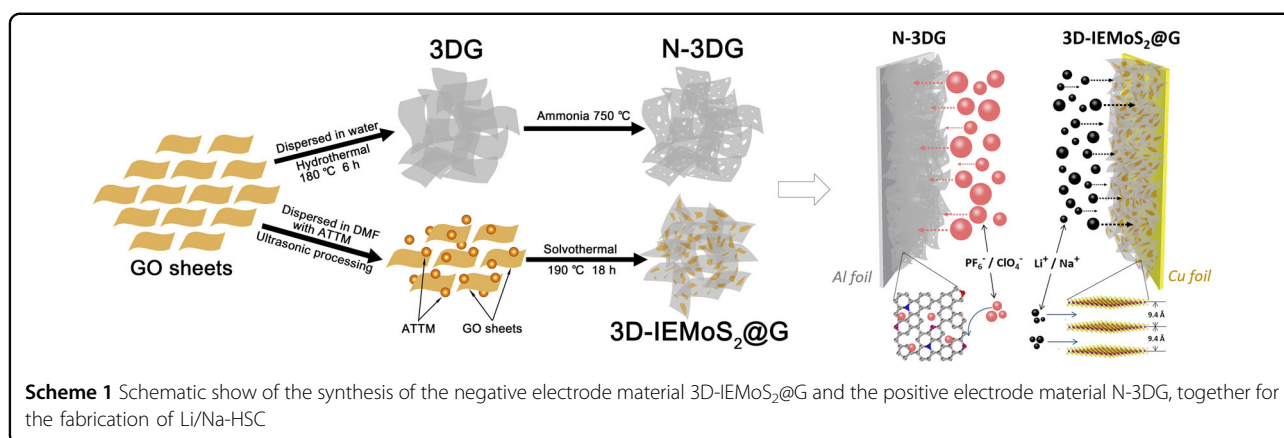
Electrochemical measurements

A LAND battery tester (Jinnuo Electronics Co., Wuhan, China) was used to perform the GC tests of the LIB and SIB half cells. The voltage windows were 0.01–3 V vs. Li/Li⁺ and Na/Na⁺, respectively. An Arbin-BT2000 test station was used to test the GC measurements of the symmetric supercapacitors and hybrid devices. The voltage window for the symmetric supercapacitors was 0–2.7 V, while the voltage window for the hybrid devices was 1–4.3 V. CV tests were performed using a VSP-300 electrochemical analyzer. Electrochemical impedance spectroscopy (EIS) was performed at an AC amplitude of 10 mV in the range of 100 kHz to 10 mHz.

Results and discussion

Characterization of 3D interlayer-expanded MoS₂/rGO nanocomposite as anode materials for both LIBs and SIBs

The 3D interlayer-expanded MoS₂/rGO nanocomposite (3D-IEMoS₂@G) was prepared by the simple solvothermal method shown in Scheme 1. The X-ray diffraction (XRD) pattern of the as-prepared 3D-IEMoS₂@G is presented in Fig. 1a, which is obviously different from that of pristine 2H-MoS₂ (JCPDS Card No. 77-1716, Fig. S1 in ESM). Calculated from the distinct peak at low angle corresponding to (002), the *d* spacing on the *c* axis of the obtained sample is 9.4 \AA , which is much larger than that of bulk 2H-MoS₂ (6.15 \AA). This phenomenon was observed by Yugang Sun²⁴ et al. and ascribed to the



intercalation of oxidized DMF species into the two S–Mo–S layers, and the peak at $2\theta \approx 32.7^\circ$ was reasonably explained by the stacking faults of the MoS₂ layer. Moreover, the XRD pattern of 3D-IEMoS₂@G closely

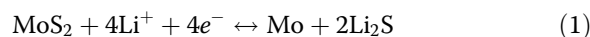
agreed with the result calculated using an interlayer spacing of 9.4 \AA ²⁴, suggesting the interlayer-expanded structure of MoS₂. When used as the anode material for Li/Na-ion batteries, such large interlayer spacing may

benefit the rate performance by allowing rapid ion transfer, especially for Na ions, which have a larger radius¹⁵. However, such intercalation of oxidized DMF species are not thermally stable. The XRD pattern and HRTEM image of 3D-IEMoS₂@G annealed at 800 under Ar atmosphere are shown in Fig. S2. It can be observed in Fig. S2a that the (002) peak shifted from $2\theta = 9.4^\circ$ to 14.2° , indicating the structural collapse of the oxidized DMF-intercalated interlayer-expanded MoS₂, which is further verified in the HRTEM image in Fig. S2b. The Raman spectrum of 3D-IEMoS₂@G is shown in Fig. 1b. The bands observed at approximately 376 cm^{-1} and 402 cm^{-1} are attributed to the in-plane (E_{2g}^1) and out-of-plane (A_{1g}) Mo-S mode in layered MoS₂, respectively^{24,25}. The characteristic G and 2D peaks of graphene were observed at 1581 cm^{-1} and 2673 cm^{-1} , indicating the presence of graphene²⁵. Meanwhile, a distinct D band was observed at 1344 cm^{-1} , and the D/G intensity ratio was ~ 1.6 , suggesting the partial reduction of graphene oxide during the solvothermal reaction process. Furthermore, XPS measurements were also performed to examine the chemical surface properties of the as-prepared 3D-IEMoS₂@G, as shown in Fig. 1c, d. As we can see, both Mo and S can be fit perfectly to a single oxidation state in the high-resolution spectra, confirming the Mo⁴⁺ and S²⁻ valence states²⁶. The integral peak area of the two elements is Mo: S $\approx 1:2.06$, corresponding to the stoichiometric ratio of MoS₂.

The morphology of the as-prepared sample is shown in Fig. 2. In Fig. 2a, b, a curved, thin, flaky morphology composed of parallelly grown MoS₂ sheets on rGO was observed by SEM, and no nanoparticles were formed, which suggests that the rGO sheets stabilize the MoS₂ sheets, forming a uniform 3D structure consisting of

nanosheets rather than aggregating into particles²⁰. In the TEM images in Fig. 2c, d, we can see a layered structure composite, and in the selected-area diffraction (SEAD) patterns inset in Fig. 2c, diffraction rings and diffraction spots corresponding to crystalline MoS₂ and rGO, respectively, were observed. In Fig. 2d, we can see the collected patterns observed in the HRTEM images are highly consistent with the XRD results, confirming the interlayer-expanded structure along the *c* axis. Energy spectrum analysis (TEM-EDS) was also performed, and the results are shown in Fig. S3. The distribution of Mo, S, and C was highly consistent with the corresponding image shape, implying the homogeneity of the composite.

The electrochemical performance of the as-prepared 3D-IEMoS₂@G as the anode material for a LIB and SIB is depicted in Fig. 3. From the cyclic voltammetry (CV) results shown in Fig. 3a, b, two series of similar-shaped curves in the initial 1st, 2nd, and 5th cycles appear in the scans of both the LIB and SIB. In the first cathodic sweep, two peaks (0.7 V and 0.3 V for the LIB; 1.1 V and 0.25 V for the SIB) were found, corresponding to the formation of Li_{*x*}MoS₂/Na_{*x*}MoS₂ and the reversible conversion reaction (MoS₂ decomposed into Mo and Li₂S/Na₂S), respectively¹¹. The broad peak near 0 V was ascribed to electrolyte decomposition, which formed a solid electrolyte interphase (SEI) layer, and the inevitable ion intercalation of rGO¹⁸. In the subsequent 2nd and 5th cathodic sweeps, two peaks at 1.5 V and 0.4 V were found in the LIB scan, corresponding to the formation of Li_{*x*}MoS₂ and the reversible conversion reaction:¹⁴



Nevertheless, three peaks appeared at 1.5 V, 0.8 V, and 0.2 V in the SIB scan, which may be due to the two-step reaction mechanism²⁷ of Na_{*x*}MoS₂ and the following conversion reaction. The two peaks observed during the anodic sweep of both the LIB and SIB are associated with the ion extraction process and the oxidation of Mo to MoS₂¹⁹. The area of the CV curve of the LIB is clearly much larger than that of the SIB, suggesting the higher specific capacity of 3D-IEMoS₂@G in the LIB than in the SIB, which was confirmed by the galvanostatic discharge/charge (GDC) results displayed in Fig. 3c, d. Several potential plateaus that were highly consistent with the peaks in Fig. 3a, b were found in the GDC curves. Although the conversion reaction formulas of MoS₂ with Li⁺ or Na⁺ are the same, the reversible specific capacity revealed a significant difference between 3D-IEMoS₂@G in the LIB (1210 mAh g⁻¹) and in the SIB (585 mAh g⁻¹). This difference may be codetermined by the more complex micropore intercalation reactions of lithium ions and the redox potential of alkali metals (Li: -3.0401 V vs. SHE; Na: -2.71 V vs. SHE), which result in the conversion depth difference between Li⁺ and Na⁺. Namely, in the following

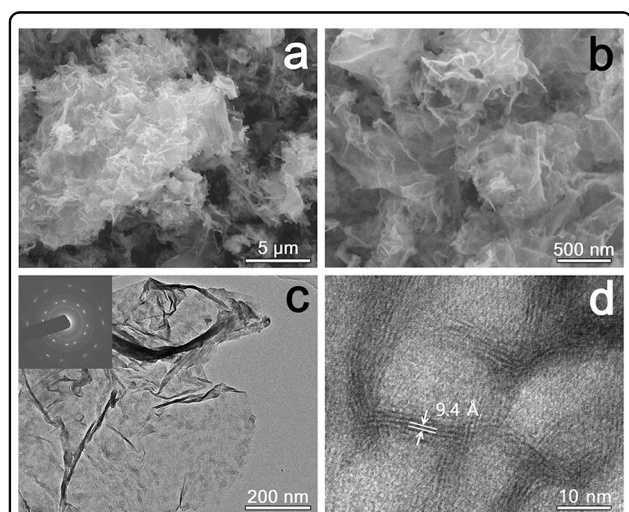
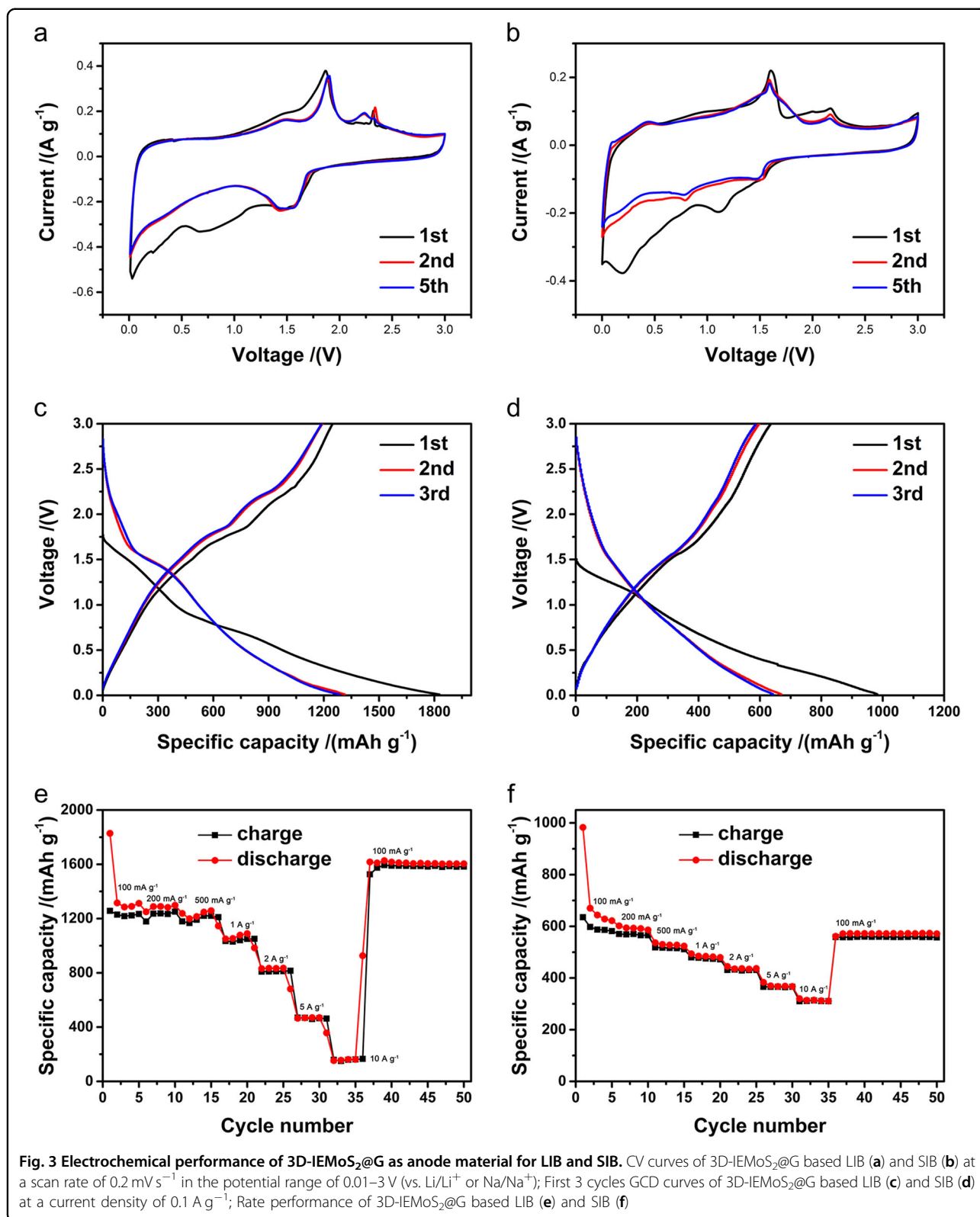
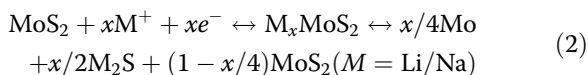


Fig. 2 Morphology of 3D-IEMoS₂@G. SEM images of 3D-IEMoS₂@G (a, b); TEM images of 3D-IEMoS₂@G (c, d)



reaction equation, the x value is larger for a LIB:



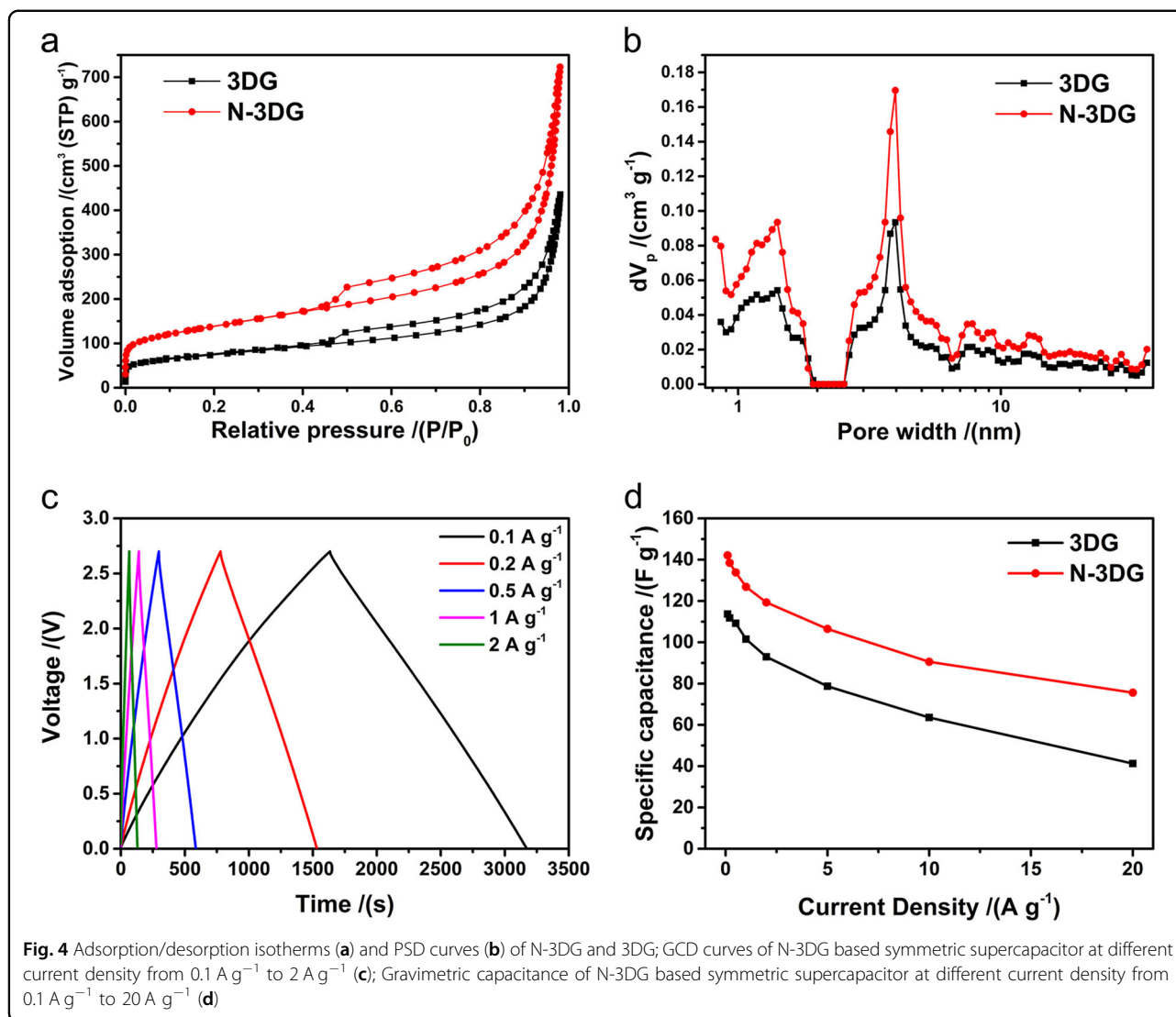
The deeper conversion level leads to the high specific capacity of the 3D-IEMoS₂@G-based LIB but results in decreased rate performance, as shown in Fig. 3e, f. Both the 3D-IEMoS₂@G-based LIB and SIB exhibit superior rate performance due to the optimized 3D graphene electron conductive network and the expanded layered structure, which allow rapid ion transfer. For comparison, the electrochemical performances of the LIB and SIB based on annealed 3D-IEMoS₂@G with a pristine interlayer spacing were also tested, and the results are shown in Fig. S4. We can see an obvious performance decline in both the LIB and SIB after annealing treatment, indicating the significance of the interlayer-expanded structure in the activation of active sites and extension of the diffusion pathway. Specifically, in Fig. 3e, the 3D-IEMoS₂@G-based LIB exhibits high specific capacity at current densities below 2 A g⁻¹, and when the current continued to increase to 5 A g⁻¹ and 10 A g⁻¹, the capacity of the LIB decreased sharply, which was possibly associated with the micropore intercalation reaction and deeper conversion level and thereby structural collapse as well as mobility decline in the low-potential range. While the 3D-IEMoS₂@G-based SIB demonstrated ultrahigh rate performance, even at a high current density of 10 A g⁻¹, it still maintained a considerable specific capacity of 315 mAh g⁻¹, with a retention of over 53% with an over 100-fold increase in current density. To preliminarily verify our assumption, another rate performance measurement of the 3D-IEMoS₂@G-based LIB was performed in the voltage range of 0.3–3 V, avoiding the low-potential range, and the results are shown in Fig. S5. As shown in Fig. S5, the 3D-IEMoS₂@G-based LIB over the partial voltage range (LIB-P) exhibited a lower specific capacity but better rate performance, which closely resembled the results of the SIB. Moreover, the LIB discharge rate performances of 3D-IEMoS₂@G, IEMoS₂ synthesized by a simple solvothermal reaction of ATTM in DMF, and a 3D graphene framework (3DGF) prepared by the solvothermal reaction of GO in DMF are displayed in Fig. S6. Both IEMoS₂ and 3DGF exhibited large performance gaps with 3D-IEMoS₂@G, indicating the synergy between IEMoS₂ and 3DGF.

Characterization of nitrogen-doped 3D graphene as a supercapacitor electrode material

Nitrogen-doped 3D graphene (N-3DG) was prepared by hydrothermal synthesis of GO and subsequent ammonia activation treatment, as shown in Scheme 1. The morphology of N-3DG is shown in Fig. S7. As the SEM images in Fig. S7a and b show, N-3DG exhibits a 3D structure

built of graphene nanosheets, and the graphene sheets are deformed after activation with ammonia. Moreover, unordered graphene sheets and a number of pores etched by ammonia can be found in the TEM images in Fig. S7c and d. The Raman spectrum in Fig. S8a revealed that the characteristic G and 2D peaks of graphene were observed at 1588 cm⁻¹ and 2670 cm⁻¹, respectively¹². Meanwhile, the distinct D band suggests that N-3DG maintains a certain amount of defects, which are ascribed to the nitrogen doping and incomplete reduction during the high-temperature ammonia activation process. The XPS results further confirm the nitrogen doping and reduction effects, which are summarized in Fig. S8b, c, d and Table S1. After the high-temperature ammonia treatment, the oxygen content in the 3D graphene structure dropped from 8.63 at% to 2.16 at%, and 3.33 at% nitrogen was doped into the graphene sheets. The high-resolution O 1s spectrum can be resolved into three individual peaks corresponding to COOH (536.8 eV), C–O (533.8 eV) and C = O (531.9 eV)²⁸. Similarly, in Fig. S8d, the N present can be classifying into pyridinic N at 398.1 eV, pyrrolic N at 399.3 eV, graphitic N at 400.9 eV and pyridinic N–O at 406 eV²⁹, indicating that nitrogen was doped uniformly into both the edge and in-plane sites of graphene carbon atoms. Pyridinic N could be oxidized to pyridinic nitrogen during oxidation and thereby provide some redox pseudocapacitance²⁹, and graphitic N may significantly improve the wettability with organic electrolyte, modify the polarity and electron distribution and thereby enhance the conductivity of the materials.

To investigate the pore structure of the as-prepared samples, N₂ adsorption/desorption was performed at 77 K. The adsorption/desorption isotherms and the corresponding PSD curves of N-3DG and 3DG are shown in Fig. 4a, b. We can see that both 3DG and N-3DG exhibit typical type IV isotherms with an H4 hysteresis loop. The uptake below $P/P_0 = 0.01$ was ascribed to adsorption by micropores, and the H4 hysteresis loop was caused by predominantly slit mesopores³⁰. Thus, N-3DG, which possess a similar isotherm but higher uptake and larger hysteresis loop, has more micropores and mesopores than 3DG. Such conclusion was further confirmed by the PSD curves in Fig. 4b and the SSA information summarized in Table S1. Both 3DG and N-3DG show a bimodal distribution, corresponding to micropores ~1.5 nm in size and mesopores ~4 nm in size. Such hierarchical porous structure can be advantageous in supercapacitor applications due to the large number of energy storage sites provided by the micropores and the high-speed ion transport paths provided by the mesopores. N-3DG exhibits a more developed pore structure and a nearly twice as large SSA of 513 m² g⁻¹ than the 3DG sample (257 m² g⁻¹), indicating the activation effect of the ammonia treatment.



To investigate the EDLC performance of N-3DG, a symmetric supercapacitor was assembled with LiPF_6 -based organic electrolyte. The galvanostatic charge/discharge (GCD) curves of the N-3DG-based symmetric supercapacitor at different current densities are shown in Fig. 4c. All curves exhibit a highly linear shape, indicating the good EDLC behavior. In addition, as the current density increased from 0.1 A g^{-1} to 2 A g^{-1} , no obvious IR drop was observed, indicating the superior electronic conductance of the graphitic carbon sheets and the enhancement effect of in-plane nitrogen doping. The rate performances of the symmetric supercapacitors assembled from 3DG and N-3DG are shown in Fig. 4d. Due to the more abundant pore structure and nitrogen doping, hierarchical porous N-3DG exhibited a superior performance over 3DG. Specifically, the specific capacitance at 0.1 A g^{-1} rose from 114 F g^{-1} to 142 F g^{-1} after activation, which was mainly ascribed to the increase in micropores

and inevitable pseudocapacitance contributed by the nitrogen and oxygen functional groups²⁹. Moreover, the capacitance retention at a high current of 20 A g^{-1} was increased from 36% (41 F g^{-1}) to 53% (75 F g^{-1}), which is associated with the increased ion transport paths due to the mesopores and the electronic conductance caused by nitrogen doping. Hence, the as-prepared N-3DG shows good EDLC performance and could be a promising positive electrode material for HSCs.

Hybrid supercapacitor based on the 3D-IEMoS₂@G nanocomposite and N-3DG

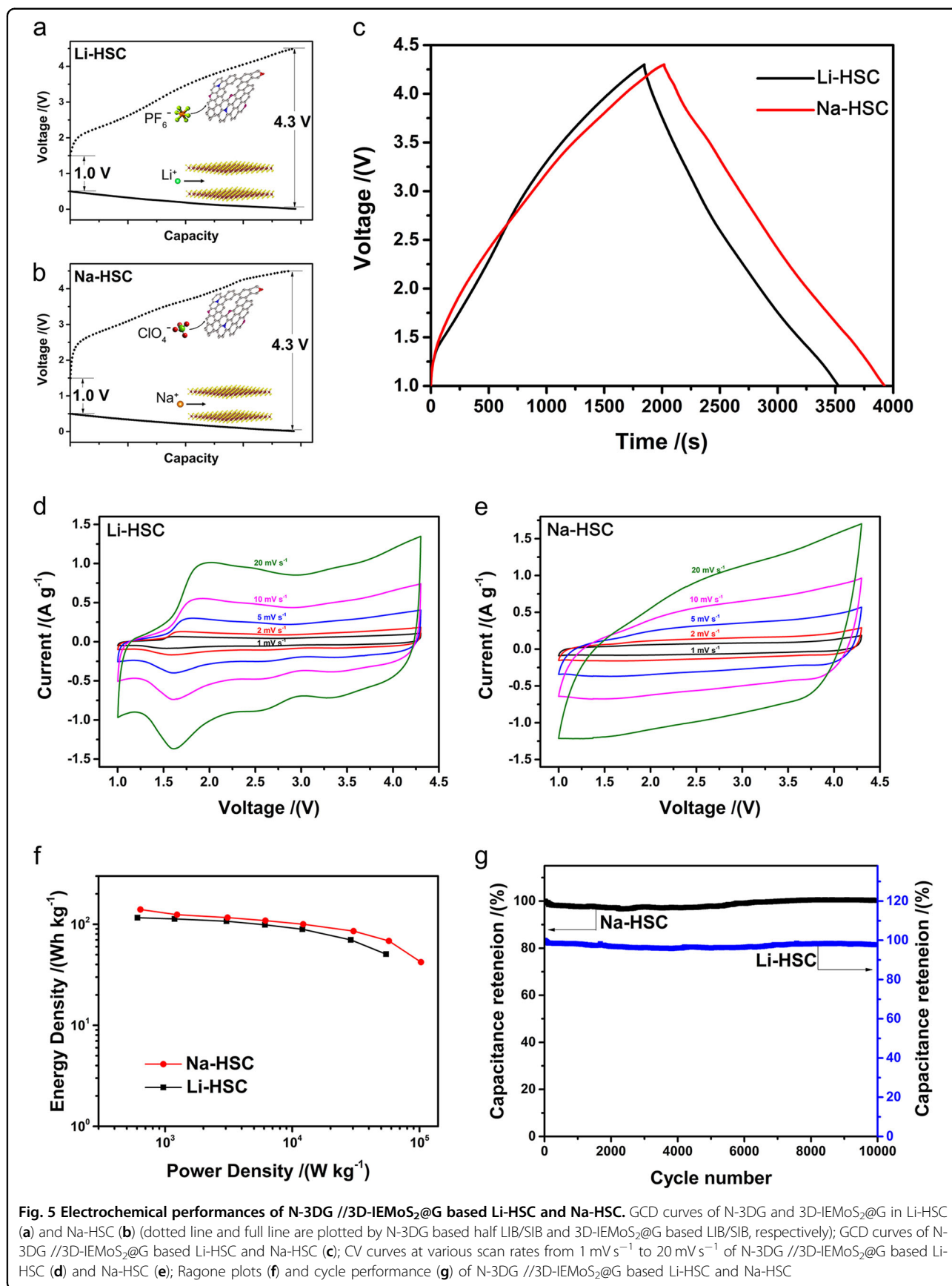
A Li-HSC and Na-HSC were fabricated from as-prepared N-3DG and 3D-IEMoS₂@G in LiPF_6 or NaClO_4 -containing organic electrolyte. To optimize the voltage window of the HSC, the 3D-IEMoS₂@G anode was prelithiated or presodiated in half cells terminating at potential of $\sim 0.5 \text{ V}$ vs. Li/Li^+ or Na/Na^+ , and details of

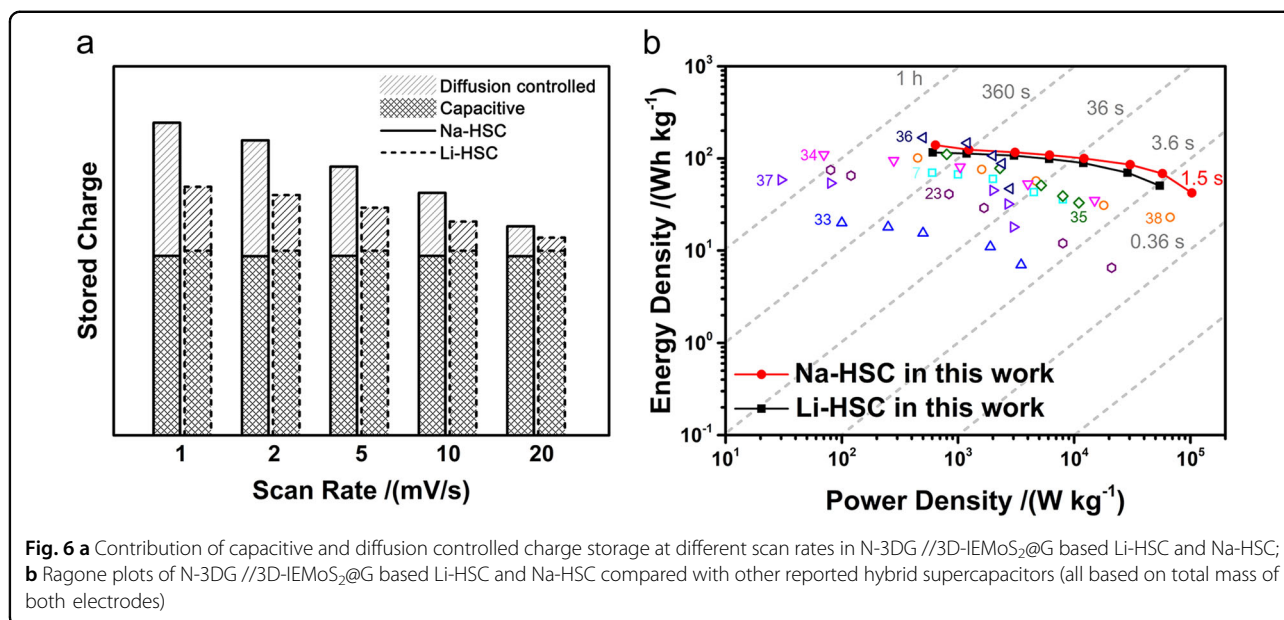
the prelithiation and presodiation processes are given in the ESM. Moreover, to maximize the energy and power performance of such hybrid devices, the working potential range and mass ratio of the two electrodes were carefully adjusted. Galvanostatic charge/discharge analysis of half cells assembled from N-3DG and lithium/sodium metal in a high voltage window of 1–4.5 V was performed to estimate the EDLC behavior of N-3DG, and the results are shown in Fig. S9. Both the N-3DG-based LIB and SIB exhibit a specific capacity of approximately 105 mAh g^{-1} and linear curves in the high potential range of 1.5–4.5 V. To avoid the precipitation of Li/Na metal and the resulting potential safety hazard, hybrid devices assembled from N-3DG and 3D-IEMoS₂@G were ultimately measured under a conservative voltage window of 1–4.3 V. The GCD curves of the N-3DG//3D-IEMoS₂@G-based Li-HSC and Na-HSC are shown in Fig. 5. During the charge process, the positive electrodes mainly underwent an adsorption reaction of PF_6^- or ClO_4^- with a linear increase in potential from 2 V to 4.5 V, along with the accumulation of charges. In addition, conversion reactions occurred in negative electrode, resulting in a smooth potential platform from 0.5 V to near 0 V. As a result, the hybrid devices exhibited nearly linear GCD curves over a voltage window of 1–4.3 V, resembling those of the N-3DG//N-3DG symmetric capacitors owing to the smooth platform with the low potential of prelithiated or presodiated 3D-IEMoS₂@G.

Furthermore, to satisfy the charge balance of the two electrodes ($Q_+ = Q_-$, namely, $m_+q_+ = m_-q_-$, where Q is the capacity, q is the specific capacity, and m is the mass of the active materials), the mass ratio of the active materials of N-3DG:3D-IEMoS₂@G was carefully adjusted from 1:3 to 1:7 (Fig. S10) due to the huge specific capacity difference of the anode and cathode materials. When the mass ratios of the active materials of N-3DG:3D-IEMoS₂@G were 1:5 and 1:6, the as-fabricated Li-HSC and Na-HSC exhibited optimum energy and power performance, respectively. Hence, these ratios were selected in this work, and all tests were performed under these optimum ratios.

The electrochemical performances of the N-3DG//3D-IEMoS₂@G-based Li-HSC and Na-HSC are shown in Fig. 5. Figure 5d, e shows the CV curves at various scan rates for Li-HSC and Na-HSC, respectively. Both curves show rectangular shapes at low scan rates, owing to the rapid ion diffusion and sufficient charge transfer resulting from the 3D-IEMoS₂@G anode led by the interlayer-expanded structure and 3D graphene skeleton frame. However, as the scan rates increased, the CV curve of Li-HSC gradually deviated from the ideal rectangular shape, due to the poor rate performance of 3D-IEMoS₂@G as the lithium-ion host anode. The CV curve of Na-HSC, by contrast, was not seriously distorted, which is ascribed to

the excellent rate performance of 3D-IEMoS₂@G in the SIB and the synergistic effect of the two electrodes. Meanwhile, the RC time constant ($\tau = RC$)³¹ was calculated to be 2.5 s for Li-HSC and 3.7 s for Na-HSC, which is comparable to that of carbon-based EDLCs (~ 1 s), further confirming the excellent power performance of the HSCs. Ragone plots (energy density vs. power density, calculated from the total mass of the two electrodes) of Li-HSC and Na-HSC are displayed in Fig. 5f. It can be visually observed that both hybrid devices show high energy densities of over 100 Wh kg^{-1} as well as high power densities of over $50,000 \text{ W kg}^{-1}$. Na-HSC exhibits an overall higher curve than Li-HSC, acquiring a high energy density of 140 Wh kg^{-1} at 630 W kg^{-1} and 43 Wh kg^{-1} at an ultrahigh power density of 103 kW kg^{-1} (charge finished within 1.5 s). The reason why the performance of the 3D-IEMoS₂@G-based Na-HSC surpassed that of the Li-HSC may be ascribed to the superior rate performance of 3D-IEMoS₂@G as a sodium-ion host anode, especially in the low-potential range. In addition, the quantitative contribution of the negative electrode in the HSC is evaluated in the kinetic analysis section. Figure 5g shows the cycle performance of the as-prepared hybrid devices. Because the interlayer-expanded structure allowed rapid ion diffusion and because of the conductive graphene network, the hybrid devices exhibited excellent cycle stability: Li-HSC maintains 97% of its capacitance after 10000 cycles, and furthermore, Na-HSC exhibits an outstanding capacitance retention rate of over 99% after 10,000 cycles. The Nyquist plots from the EIS of the 3D-IEMoS₂@G electrode before and after cycling in Li-HSC and Na-HSC are shown in Fig. S11. The plots show semicircles in the medium-frequency region ascribed to the charge transfer resistance (R_{ct}) and a line in the low-frequency region corresponding to the ion diffusion resistance. The R_{ct} of both Li-HSC and Na-HSC decreased obviously after cycling (drop from 546Ω to 333Ω for Li-HSC and from 684Ω to 468Ω for Na-HSC), indicating the structural stability of the electrode material over 10,000 cycles. Moreover, the 3D-IEMoS₂@G negative electrodes in Li-HSC and Na-HSC were further observed by SEM and TEM after cycling, and the results are shown in Fig. S12. It can be seen from the SEM images that both 3D-IEMoS₂@G electrodes in Li-HSC and Na-HSC were covered with a SEI layer and the 3D structure of the graphene skeleton was well preserved without collapse after 10,000 cycles, which ensures fast ion diffusion and electron transport during the charge/discharge process. The HRTEM images in Fig. S12 e and f show that the lattice fringes of IEMoS₂ disappeared after cycling in both Li-HSC and Na-HSC, which reveal that MoS₂ inevitably transformed into the amorphous phase during cycling. However, the





composite structure was well maintained, which can avoid the shedding of active materials and thereby the resulting capacity fading.

To further understand the effectiveness of the two electrodes in the hybrid devices, a quantitative kinetics analysis, as reported by Dunn³², was performed on the HSCs in this work (details in the ESM). The quantified capacitive and diffusion charge storage in the 3D-IEMoS₂@G-based Li-HSC and Na-HSC are shown in Fig. S13. Solid lines were drawn in the original CV plots at a scan rate of 2 mV s⁻¹, and the shaded area was calculated by $k_1 v$, representing the capacitive charge storage mechanism, which is mainly due to the N-3DG positive electrode charge storage process. The shaded areas of both samples are almost equal, while the percentage of such capacitive charge in Li-HSC (76.8%) is much higher than that in Na-HSC (60.7%). Namely, the performance gap between Li-HSC and Na-HSC is caused by the impact of the negative electrode in the HSC.

The contributions of capacitive and diffusion-controlled charge storage at different scan rates are summarized in Fig. 6a. In accordance with the trend in the Ragone plots, Na-HSC stores more charge than Li-HSC. The capacitive contributions, which is invariant with scan rate, of Li-HSC and Na-HSC are similar, while the diffusion-controlled charge storage in Na-HSC is much higher than that in Li-HSC, which is caused by the microstructure of the materials and system matching. When used as the host anode material, as-prepared 3D-IEMoS₂@G can provide numerous active sites, allowing rapid charge transfer and ion diffusion for both Li⁺ and Na⁺ by virtue of its optimized interlayer-expanded nanostructure and 3D conductive network. Therefore, 3D-IEMoS₂@G exhibits

superior performance as the anode material in LIBs and SIBs. However, due to the more complex micropore intercalation reactions of lithium ions and the intrinsic reaction features, the 3D-IEMoS₂@G-based LIB shows weak rate performance at potentials below 0.5 V, which restricts its impact in HSCs, resulting in the performance surpassing of Na-HSC. In conclusion, to fabricate a high-performance HSC, the positive material should maintain its optimized pore structure to obtain a sufficient number of adsorption sites and ion pathways. Meanwhile, the negative electrode should provide a highly effective charge transfer network and ion diffusion pathways to ensure sufficient rate performance at low potential. In addition selecting and optimizing the materials, which we do regularly, matching the components in the system is also a feasible method to meet such demands. For example, in this work, we successfully prepared a 3D interlayer-expanded MoS₂/rGO composite, but its outstanding LIB anode performance could not be effectively utilized in hybrid devices. Hence, we replaced lithium ions with sodium ions, which led to fewer side reactions and better stability, and finally realized a 3D-IEMoS₂@G-based Na-HSC with high energy density, ultrahigh power density and remarkable cycle stability. As shown in the plots in Fig. 6b, compared with porous graphene macroform//Li₄Ti₅O₁₂ (Li⁺)⁷, porous nitrogen-doped carbon//TiC (Li⁺)³³, LiNi_{0.5}Mn_{1.5}O₄//AC (Li⁺)³⁴, peanut-shell-derived nanosheets carbon//N- and O-functionalized carbon (Na⁺)³⁵, peanut-shell-derived carbon//Na₂Ti₃O₇ (Na⁺)³⁶, macroporous graphene//nanoporous disordered carbon (Na⁺)³⁷, AC//Na₂Ti₃O₇ (Na⁺)³⁸, and rGO nanocomposites//Nb₂O₅@carbon (Na⁺)²³, the system in this study shows great promise.

Conclusion

In summary, a well-structured 3D interlayer-expanded MoS₂/rGO nanocomposite was successfully synthesized, and it exhibited excellent performance as the anode in both LIBs and SIBs due to its characteristic interlayer-expanded structure. When coupled with N-3DG to fabricate an organic HSC, the 3D-IEMoS₂@G-based Na-HSC showed high energy density (140 Wh kg⁻¹ at 630 W kg⁻¹), excellent cycling stability (over 99% capacitance retention after 10,000 cycles) and outstanding power density (43 Wh kg⁻¹ at 103 kW kg⁻¹, discharge finished within 1.5 s), surpassing the Li-HSC with the same material system. Combining the electrochemical results of variable ions of Li⁺ or Na⁺ and the quantitative kinetics analysis of the CV curves, we conclude that matching the structure of the materials and ions, which could lead to the high performance of the anode at low potential, is a key issue to adequately exploit the synergistic effect of the two electrodes with different mechanisms and thereby fabricate high-performance HSCs.

Acknowledgements

This work was supported by the National Natural Science Foundation of China (grant No. 51672151) and 973 program of China (No.2014CB932401).

Author details

¹State Key Laboratory of New Ceramics and Fine Processing, School of Materials Science and Engineering, Tsinghua University, 100084 Beijing, China. ²Key Laboratory of Advanced Materials (MOE), School of Materials Science and Engineering, Tsinghua University, 100084 Beijing, China. ³Engineering Laboratory for Functionalized Carbon Materials, Graduate School at Shenzhen, Tsinghua University, 518055 Shenzhen, China

Conflict of interest

The authors declare that they have no conflict of interest.

Publisher's note

Springer Nature remains neutral with regard to jurisdictional claims in published maps and institutional affiliations.

Supplementary information is available for this paper at <https://doi.org/10.1038/s41427-018-0073-y>.

Received: 16 April 2018 Revised: 23 June 2018 Accepted: 2 July 2018.

Published online: 20 August 2018

References

- Peng, H.-J., Huang, J.-Q. & Zhang, Q. A review of flexible lithium-sulfur and analogous alkali metal-chalcogen rechargeable batteries. *Chem. Soc. Rev.* **46**, 5237–5288 (2017).
- Balogun, M.-S., Luo, Y., Qiu, W., Liu, P. & Tong, Y. A review of carbon materials and their composites with alloy metals for sodium ion battery anodes. *Carbon* **98**, 162–178 (2016).
- Stephenson, T., Li, Z., Olsen, B. & Mitlin, D. Lithium ion battery applications of molybdenum disulfide (MoS₂) nanocomposites. *Energy Environ. Sci.* **7**, 209–231 (2014).
- Li, H. et al. Ultra-thick graphene bulk supercapacitor electrodes for compact energy storage. *Energy Environ. Sci.* **9**, 3135–3142 (2016).
- Yu, X. et al. Ultrahigh-rate and high-density lithium-ion capacitors through hybridizing nitrogen-enriched hierarchical porous carbon cathode with prelithiated microcrystalline graphite anode. *Nano Energy* **15**, 43–53 (2015).
- Ding, J. et al. Peanut shell hybrid sodium ion capacitor with extreme energy-power rivals lithium ion capacitors. *Energy Environ. Sci.* **8**, 941–955 (2015).
- Ye, L. et al. A high performance Li-ion capacitor constructed with Li₄Ti₅O₁₂/C hybrid and porous graphene macroform. *J. Power Sources* **282**, 174–178 (2015).
- Zhang, S. et al. High performance lithium-ion hybrid capacitors employing Fe₃O₄-graphene composite anode and activated carbon cathode. *ACS Appl. Mater. Interfaces* **9**, 17136–17144 (2017).
- Luo, J. et al. Pillared structure design of MXene with ultralarge interlayer spacing for high-performance lithium-ion capacitors. *ACS Nano* **11**, 2459–2469 (2017).
- Zhang, J., Liu, X., Wang, J., Shi, J. & Shi, Z. Different types of pre-lithiated hard carbon as negative electrode material for lithium-ion capacitors. *Electrochim. Acta* **187**, 134–142 (2016).
- Hwang, H., Kim, H. & Cho, J. MoS₂ nanoplates consisting of disordered graphene-like layers for high rate lithium battery anode materials. *Nano Lett.* **11**, 4826–4830 (2011).
- Xu, Y. et al. Holey graphene frameworks for highly efficient capacitive energy storage. *Nat. Commun.* **5**, 4554 (2014).
- Zeng, X. et al. Hierarchical nanocomposite of hollow N-doped carbon spheres decorated with ultrathin WS₂ nanosheets for high-performance lithium-ion battery anode. *ACS Appl. Mater. Interfaces* **8**, 18841–18848 (2016).
- Zhang, X. et al. SnS₂ nanoflakes anchored graphene obtained by liquid phase exfoliation and MoS₂ nanosheet composites as lithium and sodium battery anodes. *Electrochim. Acta* **227**, 203–209 (2017).
- Zhao, C. et al. Enhanced sodium storage capability enabled by super wide-interlayer-spacing MoS₂ integrated on carbon fibers. *Nano Energy* **41**, 66–74 (2017).
- Sun, D. et al. MoS₂/graphene nanosheets from commercial bulky MoS₂ and graphite as anode materials for high rate sodium-ion-batteries. *Adv. Energy Mater.* **8**, 1702383 (2018).
- Cook, J. B. et al. Pseudocapacitive charge storage in thick composite MoS₂ nanocrystal-based electrodes. *Adv. Energy Mater.* **7**, 1601283 (2016).
- Chang, K. & Chen, W. L-cysteine-assisted synthesis of layered MoS₂/graphene composites with excellent electrochemical performances for lithium ion batteries. *ACS Nano* **5**, 4720–4728 (2011).
- Park, S.-K. et al. Scalable synthesis of few-layer MoS₂ incorporated into hierarchical porous carbon nanosheets for high-performance Li- and Na-ion battery anodes. *ACS Appl. Mater. Interfaces* **8**, 19456–19465 (2016).
- Xie, X., Ao, Z., Su, D., Zhang, J. & Wang, G. MoS₂/graphene composite anodes with enhanced performance for sodium-ion batteries: the role of the two-dimensional heterointerface. *Adv. Funct. Mater.* **25**, 1393–1403 (2015).
- Pan, H., Hu, Y.-S. & Chen, L. Room-temperature stationary sodium-ion batteries for large-scale electric energy storage. *Energy Environ. Sci.* **6**, 2338–2360 (2013).
- Hwang, J.-Y., Myung, S.-T. & Sun, Y.-K. Sodium-ion batteries: present and future. *Chem. Soc. Rev.* **46**, 3529–3614 (2017).
- Lim, E. et al. High-performance sodium-ion hybrid supercapacitor based on Nb₂O₅@carbon core-shell nanoparticles and reduced graphene oxide nanocomposites. *Adv. Funct. Mater.* **26**, 3711–3719 (2016).
- Gao, M.-R., Chan, M. K. Y. & Sun, Y. Edge-terminated molybdenum disulfide with a 9.4-Å interlayer spacing for electrochemical hydrogen production. *Nat. Commun.* **6**, 7493 (2015).
- Li, Y. et al. MoS₂ nanoparticles grown on graphene: an advanced catalyst for the hydrogen evolution reaction. *J. Am. Chem. Soc.* **133**, 7296–7299 (2011).
- Kim, H.-S. et al. Oxygen vacancies enhance pseudocapacitive charge storage properties of MoO_{3-x}. *Nat. Mater.* **16**, 454–460 (2017).
- Park, J. et al. Discharge mechanism of MoS₂ for sodium ion battery: electrochemical measurements and characterization. *Electrochim. Acta* **92**, 427–432 (2013).
- Zhan, C. et al. Flour food waste derived activated carbon for high-performance supercapacitors. *RSC Adv.* **6**, 89391–89396 (2016).
- Zhan, C. et al. Nitrogen-rich hierarchical porous hollow carbon nanofibers for high-performance supercapacitor electrodes. *RSC Adv.* **6**, 41473–41476 (2016).
- Yu, X. et al. Ultrahigh-rate and high-density lithium-ion capacitors through hybridizing nitrogen-enriched hierarchical porous carbon cathode with prelithiated microcrystalline graphite anode. *Nano Energy* **15**, 43–53 (2015).
- Chen, Z. et al. High-performance sodium-ion pseudocapacitors based on hierarchically porous nanowire composites. *ACS nano* **6**, 4319–4327 (2012).

32. Augustyn, V. et al. High-rate electrochemical energy storage through Li⁺-intercalation pseudocapacitance. *Nat. Mater.* **12**, 518–522 (2013).
33. Wang, H. et al. A high-energy lithium-ion capacitor by integration of a 3D interconnected titanium carbide nanoparticle chain anode with a pyridine-derived porous nitrogen-doped carbon cathode. *Adv. Funct. Mater.* **26**, 3082–3093 (2016).
34. Arun, N. et al. Nanostructured spinel LiNi_{0.5}Mn_{1.5}O₄ as new insertion anode for advanced Li-ion capacitors with high power capability. *Nano Energy* **12**, 69–75 (2015).
35. Ding, J. et al. Heteroatom enhanced sodium ion capacity and rate capability in a hydrogel derived carbon give record performance in a hybrid ion capacitor. *Nano Energy* **23**, 129–137 (2016).
36. Li, H., Peng, L., Zhu, Y., Zhang, X. & Yu, G. Achieving high-energy–high-power density in a flexible quasi-solid-state sodium ion capacitor. *Nano Lett.* **16**, 5938–5943 (2016).
37. Wang, F. et al. A quasi-solid-state sodium-ion capacitor with high energy density. *Adv. Mater.* **27**, 6962–6968 (2015).
38. Dong, S. et al. Pseudocapacitive behaviours of Na₂Ti₃O₇@CNT coaxial nanocables for high-performance sodium-ion capacitors. *J. Mater. Chem. A* **3**, 21277–21283 (2015).